# Feature-based ensemble history matching in a fractured carbonate reservoir using time-lapse deep electromagnetic tomography

| Item Type | Article |
|---|---|
| Authors | Zhang, Yanhui;Hoteit, Ibrahim;Katterbauer, Klemens;Maucec, Marko;Marsala, Alberto F. |
| Citation | Zhang, Y., Hoteit, I., Katterbauer, K., Maucec, M., & Marsala, A. F. (2021). Feature-based ensemble history matching in a fractured carbonate reservoir using time-lapse deep electromagnetic tomography. Journal of Petroleum Science and Engineering, 109259. doi:10.1016/j.petrol.2021.109259 |
| Eprint version | Post-print |
| DOI | [10.1016/j.petrol.2021.109259](10.1016/j.petrol.2021.109259) |
| Publisher | Elsevier BV |
| Journal | Journal of Petroleum Science and Engineering |
| Rights | NOTICE: this is the author's version of a work that was accepted for publication in Journal of Petroleum Science and Engineering. Changes resulting from the publishing process, such as peer review, editing, corrections, structural formatting, and other quality control mechanisms may not be reflected in this document. Changes may have been made to this work since it was submitted for publication. A definitive version was subsequently published in Journal of Petroleum Science and Engineering, [, , (2021-07)] DOI: 10.1016/j.petrol.2021.109259 . © 2021. This manuscript version is made available under the CC-BY-NC-ND 4.0 license http://creativecommons.org/licenses/by-nc-nd/4.0/ |
| Download date | 2024-04-09 18:04:49 |

| Link to Item | http://hdl.handle.net/10754/670445 |
| --- | --- |

# Feature-based ensemble history matching in a fractured carbonate reservoir using time-lapse deep electromagnetic tomography

*Yanhui Zhang and Ibrahim Hoteit; King Abdullah University of Science and Technology*
*Klemens Katterbauer, Marko Maucec, and Alberto F. Marsala; Saudi Aramco*

## Abstract

Carbonate reservoirs typically exhibit very complex geological structures and are characterized by flow dynamics primarily occurring in fractures. The intricate network of fractures as well as their interconnectedness may lead to unexpected flow patterns and uneven sweep efficiency. Determining reservoir properties of both matrix and fracture channels is quintessential for accurately tracking the fluid front movement in the reservoir, optimizing sweep efficiency, and maximizing hydrocarbon production. In this study, we showcase the application of a feature-oriented ensemble-based history matching workflow to a complex fractured carbonate reservoir box model, focusing on the use of formation resistivity tomography data that are usually inferred from deep crosswell electromagnetic (EM) surveys. Compared with the production data that are commonly used in history matching, deep EM measurements provide additional information about the spatial distribution of subsurface reservoir properties in the interwell volumes by exploiting the strong resistivity contrast between water and hydrocarbons. A hybrid parameterization approach is used to represent the multiscale fracture distribution in which the spatial distribution of small-scale fractures is modelled by a truncated Gaussian simulation method. A large number (over one million) of uncertain model parameters including reservoir matrix and fracture properties as well as Archie's parameters are identified and updated by an iterative ensemble smoother. For an efficient integration of the high-dimensional and noisy EM tomography data, the boundary or contour information extracted from the EM resistivity field is instead assimilated through a distance parameterization approach. A modified bootstrap-based localization is proposed to regularize the model updates adaptively during the iteration to reduce sampling errors. Especially, to improve the computational efficiency in dealing with the large dimensions of both data and model parameters, the localization is implemented in a projected low-dimensional data subspace. Experimental results demonstrate the applicability and efficiency of the developed workflow for reservoir history matching in more realistic model settings. The comparative case study also illustrates the significance of jointly incorporating multiple sources of data for better quantification of model uncertainty, and the great potential of deep EM data for enhancing the characterization of complex fractured carbonate reservoirs.

**Keywords:** History matching, Ensemble methods, Adaptive localization, Distance parameterization, Fractured carbonate reservoir, EM tomography.

## Introduction

Ensemble-based assimilation methods such as the ensemble Kalman filter (EnKF) and smoother (ES) have recently received remarkable interests in various disciplines, especially for the study of large-scale geophysical systems. In petroleum industry, the applications covers many aspects including reservoir characterization, production optimization, and uncertainty quantification (Aanonsen et al., 2009; Jung et al., 2018; Oliver and Chen, 2011). Compared to conventional assisted history matching techniques, the ensemble-based assimilation methods provide an efficient and scalable framework, under which large-scale reservoir models can be easily calibrated through the integration of various types of data. Significant research has been conducted to improve the performance of these ensemble methods in dealing with more challenging and realistic inverse problems (Dovera and Della Rossa, 2011; Emerick and Reynolds, 2013; Hoteit et al., 2012; Liu et al., 2016; Lorentzen et al., 2012; Luo et al., 2015; Oliver and Alfonzo, 2018; Zhang et al., 2014). For real field case studies, Chen and Oliver (2014)) showcased a history-matching application in the Norne field using an iterative ensemble smoother, in which approximately 150,000 model parameters including permeability, porosity, net-to-gross ratio,

transmissibility, and depth of water/oil contacts were calibrated. It turned out that the ensemble-based history matching outperformed the manual counterpart with both better data match to a long production history and more plausible calibrated reservoir models. Abadpour et al. (2018) reported a successful implementation of ensemble-based history matching for a couple of giant complex reservoirs (over tens of millions of uncertain model parameters including geologic facies), demonstrating the robustness and superior performance of the ensemble methods for assisted history matching.

Recent research in reservoir characterization has shown an upward tendency of integrating multiple sources of geophysical data (e.g., time-lapse seismic and electromagnetic (EM) measurements), together with well production data (e.g., well rates and pressures), to enhance the fidelity of estimated reservoir models (Katterbauer et al., 2016; Liang et al., 2016). The motivation behind the joint integration of multiple datasets is to exploit the complementary nature of different data types in recovering reservoir properties and principal structures. For instance, complementary to the production data that typically have limited spatial coverage while high temporal frequency, time-lapse seismic and EM data possess much higher spatial resolution with additional information about dynamic changes far from well locations in the reservoir. Moreover, cross-well seismic and EM techniques, reaching deep into the reservoir and mapping formation resistivity between wells, fill an intermediate resolution gap between well logs and surface measurements (Al-Ali et al., 2009). The field studies from Marsala et al. (2017, 2008) reported that cross-well EM tomography was able to produce useful interwell resistivity and saturation mapping even at widely-spaced wells.

Compared to commonly used production data for history matching, the integration of geophysical data exhibits some distinctive features, including embedded large uncertainty that arises from the perplexing acquisition-processing-interpretation process, multiple levels at which the associated geophysical attributes can be integrated, and large dimensions. Taking the EM data for example, one has the option to history match raw EM data (after necessary data processing), inverted resistivity (from geophysical inversion), or interpreted saturation (from petrophysical inversion). No matter which level of data is selected, however, the effective exploitation of the characteristics of each data form and the proper quantification of the involved uncertainty are the key to convert the data information into valid model calibration.

Inspired by the interpretive nature of geophysical data, feature-oriented history matching approach aims to calibrate reservoir models to match the features or patterns detected from the original data. The feature may refer to a geometric extraction of spatial changes in saturation, acoustic impedance, or resistivity interpreted from seismic and EM measurements. When the features of interest can be consistently extracted, they usually retain the essential information contained in the original data. Besides, higher computational efficiency can be achieved because the feature space typically has much lower dimensions than the original data space. Leeuwenburgh and Arts (2014) introduced a distance parameterization of seismic anomalies due to saturation effects in terms of front positions. It turned out that the distance parameterization approach was able to significantly reduce the number of data while still capture the primary information carried in the original data. Zhang and Leeuwenburgh (2017) further extended this approach from the perspective of image analysis, to improve its performance in dealing with more complex reservoir conditions. Obidegwu et al. (2017) proposed a binary approach for the integration of time-lapse seismic data. In this approach, converted binary seismic gas and water maps representing the 'hardening' and 'softening' signals from observed seismic data are history matched, using the current measurement metric minimized by an evolutionary algorithm. This feature-based binary approach was indicated as a quick-look tool suitable for reservoir management. Zhang et al. (2020) examined the integration of cross-well EM data at different levels (measured magnetic-field responses and inverted formation conductivity) using ensemble methods on a synthetic channelized reservoir model. The numerical results showed that integrating the inverted resistivity field with the feature-oriented approach gave comparable performance as the direct integration of the original EM data under relatively ideal conditions. Zhang and Hoteit (2021) further extended the workflow to incorporate the joint seismic and EM inversion to reduce the interpretative ambiguities of inverted reservoir properties. From the perspective of dimensional reduction, some recent studies utilized techniques like wavelet transform (Luo et al., 2017), dictionary learning (Soares et al., 2020), and local analysis (Soares et al., 2021) to handle big seismic data. Luo et al. (2018) proposed a correlation-based localization method to overcome some limitations of distance-based localization, and applied it to regularize seismic history matching of full Norne field model (Lorentzen et al., 2019).

2

Carbonate reservoirs typically have very complex geological structures and are characterized by flow dynamics primarily occurring in fractures. The intricate network of fractures as well as their interconnectedness may lead to unexpected flow patterns and uneven sweep efficiency. It is quintessential to integrate all available information to determine reservoir properties of both matrix and fracture, in order to accurately track the fluid front movement and optimize hydrocarbon production. Conditioning fractured reservoir models to dynamic data is still a challenging research area due to the inherent complexity of fracture distribution, involved physical modelling processes, and strong nonlinearity. Sun (2011) applied the EnKF to identify the fault network geometry using production data. A multipoint geostatistical modelling algorithm was used to generate the initial ensemble of fault network realizations. Fault network geometry was indirectly inferred from the updated permeability fields. Lu and Zhang (2015) proposed a Hough-transform-based parameterization method, to facilitate the history matching process of fracture distribution by transforming it into a Gaussian random field in the Hough space. Nejadi et al. (2017) presented an integrated approach for the history matching of fractured reservoirs, in which the parameters of a discrete fracture network (DFN) model were taken as the uncertain parameters and updated with the EnKF based on production data. Yao et al. (2019) developed a hierarchical approach for multiscale fracture characterization. The large-scale fractures were parameterized by the Hough-transform-based parameterization method and modelled by an embedded discrete fracture model. The small-scale fractures were represented by a truncated Gaussian field and modelled by a dual porosity dual permeability (DPDP) model. Zhang et al. (2021) recently proposed a parameterization method for the multiscale fracture network based on a deep sparse autoencoder (DSAE). The DSAE was trained to transform the fracture network to a low-dimensional latent variables, which were then conditioned to production data using an iterative ensemble smoother.

In this study, we apply the developed feature-oriented ensemble history matching workflow to a realistic carbonate reservoir box model with a complex fracture channel network. A hybrid parameterization approach is used to represent the multiscale fracture distribution in which the spatial distribution of small-scale fractures is modelled by a truncated Gaussian simulation method. Over one million uncertain model variables including reservoir matrix and fracture properties as well as Archie's parameters are conditioned to both production and time-lapse EM data. A modified bootstrap-based Kalman gain localization is proposed to regularize the model update, in order to reduce sampling errors and increase the number of degrees of freedom to match the large amount of data. Especially, data subspace projection is implemented to improve the computational efficiency of the localization in dealing with the large model and data dimensions. Particular attention is devoted to assessing the efficacy of the developed workflow in dealing with large-scale complex reservoir applications and the potential of cross-well EM data for enhanced characterization of naturally fractured carbonate reservoirs.

## Ensemble-based reservoir history matching

History matching is known as the process in which unknown reservoir parameters are estimated to reproduce the observed historical dynamic responses. From a mathematical point of view, history matching is best described as an ill-posed large-scale inverse problem, whose solution space consists of numerous possible combinations of model variables matching the observations equally well. Therefore, it is valuable for a history matching workflow equipped with a proper assessment of uncertainty to facilitate the decision making on reservoir management and investment.

Based on Bayesian statistics, the objective of ensemble-based history matching is to approximate the posterior probability distribution of uncertain model variables, by updating the samples from their prior probability distribution using available observations. In practice, the implementation of ensemble-based history matching can be roughly divided into two stages. In the first stage, an initial ensemble of identified uncertain model parameters is generated based on available prior knowledge (e.g., well logs and seismic), typically via geological and geostatistical modelling. This is a critical step in the sense that the posterior solution lives in the subspace of the initial ensemble. It is therefore important to ensure that the initial ensemble represents the prior uncertainty properly. In the second stage, the generated model realizations are calibrated through a two-step assimilation process which consists of a forecast step and an analysis step. Because history matching is essentially a parameter estimation problem in which there are no time-varying state variables estimated. The forecast step usually involves only the forward simulation of observed responses using the current model estimate. In the analysis step, model

parameters are calibrated with a Kalman-type update equation in which the mean and the covariance are approximated by their ensemble estimates. The standard implementation of EnKF or ES without iteration has shown to be capable of dealing with some degree of nonlinearity. For strongly nonlinear problems, however, iterative extensions of these methods will be necessary in order to achieve reasonable results.

In this study, we use an iterative ensemble smoother named as LM-EnRML developed by Chen and Oliver (2013), which has shown robust performance in coping with highly nonlinear history matching problems. The updating equation in the approximate form of LM-EnRML for the $i$th realization of model parameters $\mathbf{m}_i^\ell$ with the iteration index $\ell$ (= 0, 1, …, $N_\ell$) is,

$$\mathbf{m}_i^{\ell+1} = \mathbf{m}_i^\ell + \Delta\mathbf{M}^\ell\Delta\mathbf{D}^{\ell\mathrm{T}}\big[(1+\lambda_\ell)\mathbf{I}_{N_d} + \Delta\mathbf{D}^\ell\Delta\mathbf{D}^{\ell\mathrm{T}}\big]^{-1}\mathbf{C}_D^{-\frac{1}{2}}\big[\mathbf{d}_{obs,i} - \mathbf{g}(\mathbf{m}_i^\ell)\big], \qquad (1)$$

where $\mathbf{C}_D$ is the observation error covariance matrix which is assumed to be diagonal (i.e., uncorrelated observation errors), and $\mathbf{d}_{obs,i}$ is a vector of perturbed observations obtained by adding Gaussian noise of $\mathcal{N}(\mathbf{0}, \mathbf{C}_D)$ to the original observation vector $\mathbf{d}_{obs}$. The operator $\mathbf{g}(\cdot)$ denotes the forward model (e.g., flow simulator and rock physics relationship) relating the model parameters to predicted data, and $\mathbf{I}_{N_d}$ represents the identity matrix of size $N_d$. The term $\lambda_\ell$ is the Levenberg-Marquardt (LM) tuning parameter, which controls both the step size and the search direction for each iteration. The deviation matrices $\Delta\mathbf{D}^\ell$ and $\Delta\mathbf{M}^\ell$ are computed by

$$\Delta\mathbf{D}^\ell = \frac{\mathbf{C}_D^{-\frac{1}{2}}\big(\mathbf{D}^\ell - \overline{\mathbf{D}^\ell}\big)}{\sqrt{N_e - 1}}, \qquad \Delta\mathbf{M}^\ell = \frac{\mathbf{M}^\ell - \overline{\mathbf{M}^\ell}}{\sqrt{N_e - 1}}. \qquad (2)$$

The matrices $\mathbf{M}^\ell$ and $\mathbf{D}^\ell$ denote the ensembles of model realizations $\big\{\mathbf{m}_i^\ell\big\}_{i=1}^{N_e}$ and corresponding simulated data $\big\{\mathbf{g}(\mathbf{m}_i^\ell)\big\}_{i=1}^{N_e}$, respectively. The overlined counterpart represents the mean matrix, in which each column is identical and equal to the ensemble mean. The scalar $N_d$ is the number of data, and the scalar $N_e$ is the number of ensemble members. The detail of the tuning strategy of $\lambda_\ell$ and the stopping criteria of the optimization used in the application are described in Appendix A.

**Carbonate reservoir box model**

The synthetic box model of a fractured carbonate reservoir is extracted and tailored from the geological model of an oil field. It has two horizontal wells that were drilled roughly parallel, approximately 1300 m far apart, although at different vertical levels. The reservoir has relatively high porosity while low matrix permeability. The production and recovery behavior is dominated by a multiscale fracture network as shown in Figure 1, which causes uneven water advancement with flooding predominantly taking place in high permeable fracture corridors. The large-scale fracture channels (in blue) penetrate the entire reservoir section with a long horizontal extension. They impose a strong influence on the fluid flow. The distribution of small-scale fractures (in turquoise) is often lithology-related. For the regions where small-scale fractures densely develop, they may also affect subsurface flow dynamics and production behavior.
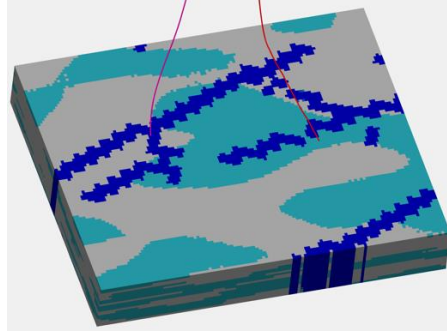
***Figure 1*** *Multiscale Fracture network (in blue for large-scale fractures and turquoise for small-scale fractures) for the carbonate reservoir box model with horizontal injector (left) and producer (right).*

Relying on well data alone, it is difficult to detect oil patches in the interwell area for further production optimization. This motivates the use of cross-well electromagnetic (EM) tomography that provides additional information about subsurface conditions far away from the wells. In a crosswell EM survey, transmitters and receivers are placed in different wells and moved to log the entire survey depth interval. The transmitter generates a primary magnetic field that is sent into the formation at predefined frequencies (Wilt et al., 1995). The primary field induces a current in conductive formations, which then generates an opposing secondary EM field. The strength of the secondary field is proportional to formation resistivity. These generated magnetic fields are finally measured by the receivers. Through EM inversion, an interwell resistivity mapping can then be obtained, from which flooded areas can potentially be identified by virtue of considerable resistivity contrast between oil and salt water.

A DPDP model is used to simulate fluid flow dynamics in the fractured carbonate reservoir box model. The simulation model has dimensions of $122 \times 100 \times 20$, covering an approximate area of $3000 \times 2500$ m$^2$ with varying layer thickness ranging approximately from 3 to 5 m. The fluid system consists of two immiscible phases, oil and brine. There is an aquifer support with water influx from the west edge of the reservoir. The injector is under bottomhole-pressure control at 5600 psi, and the producer is on a liquid rate control at 9000 stb/d. Figure 2 shows the matrix porosity and log-transformed horizontal permeability fields of the reference reservoir model.
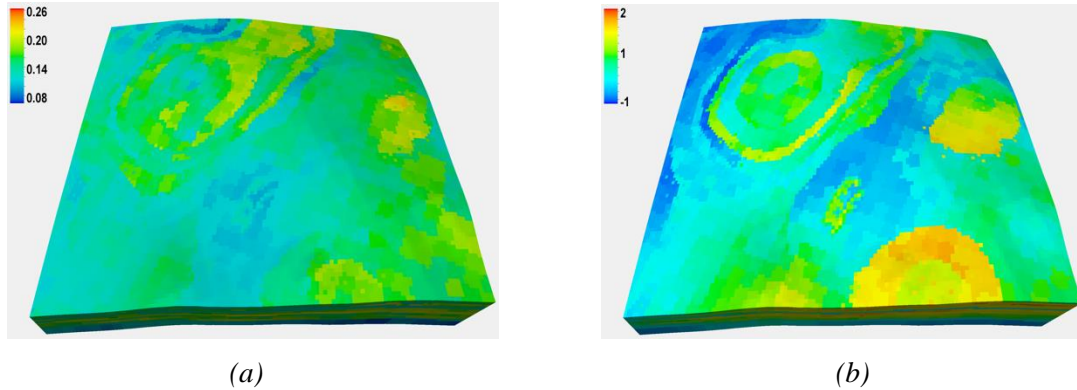


*(a)*          *(b)*

***Figure 2*** *Matrix porosity (a) and log-transformed permeability (b) fields for the reference model.*

Synthetic production and time-lapse EM data are generated from the reference reservoir model. The production data include water and oil production rates, producer bottomhole-pressure, and water injection rate. The noise in the production data is assumed to be Gaussian with zero mean and standard deviations 50 psi for the producer bottomhole-pressure, 200 stb/d for the oil production rate, 100 stb/d for the water production rate, and 500 stb/d for the water injection rate. The history matching period is 7 years during which the production data are collected every two months. Regarding the EM data, we focus on the resistivity fields that can be obtained from EM inversion in practice, but in this synthetic case they are generated directly from the reference reservoir model through rock physics

5

modeling. Archie's law (Archie, 1942) is used to quantify the relationship of formation resistivity to rock porosity and water saturation as:

$$R_t = aR_w\phi^{-m}S_w^{-n}, \tag{3}$$

where $R_t$ and $R_w$ are formation and the brine resistivity, respectively. The terms $a$, $m$ and $n$ are known as Archie's parameters, whose values generally depend on the rock's properties (e.g., pore structure, cementation, and wettability). The brine conductivity $R_w$ is computed from an empirical relationship (Dresser, 1982),

$$R_w = \left(0.0123 + \frac{3647.5}{C_w^{0.955}}\right)\frac{82}{1.8T + 39}, \tag{4}$$

where $C_w$ represents the salt concentration (in ppm), and T denotes the formation temperature (in °C). The rock physics model is linked to the fluid flow simulator from which the distributions of $S_w$ and $C_w$ are provided. The concentration of salt in the injected water is 17.52 lb/stb. Table 1 shows the values of the parameters in the rock physics model used for the reference reservoir model. Within the fracture network in the DPDP model, the resistivity is computed based on the averages between matrix and fracture properties using Archie's law.

**Table 1** *Input values of the parameters in the rock physics model.*

| $a$ | $m$ | $n$ | T |
|-----|-----|-----|------|
| 1 | 1.8 | 1.8 | 80 °C |

Resistivity fields at Year 1 and Year 7 from the reference reservoir model are collected. Considering the interpretive capability of cross-well EM data and associated inversion in practice, a subdomain enclosing the interwell region and the adjacent area surrounding well trajectories is defined to extract valid volume of resistivity from the full field as shown in Figure 3(a). Then, a 2D resistivity map is obtained from the extracted resistivity cube through simple vertical averaging. Figures 3(b) and 3(c) show the corresponding reciprocals of resistivity (namely, conductivity) maps at Year 1 and Year 7 that are used as the observations for history matching. The high resistivity contrasts illuminate water influx from the aquifer connected to the west edge of the reservoir and flooded areas by the injected water. Time-lapse changes of resistivity reflect the fact that the injected water preferentially flows through the more permeable fracture corridors to the producer.
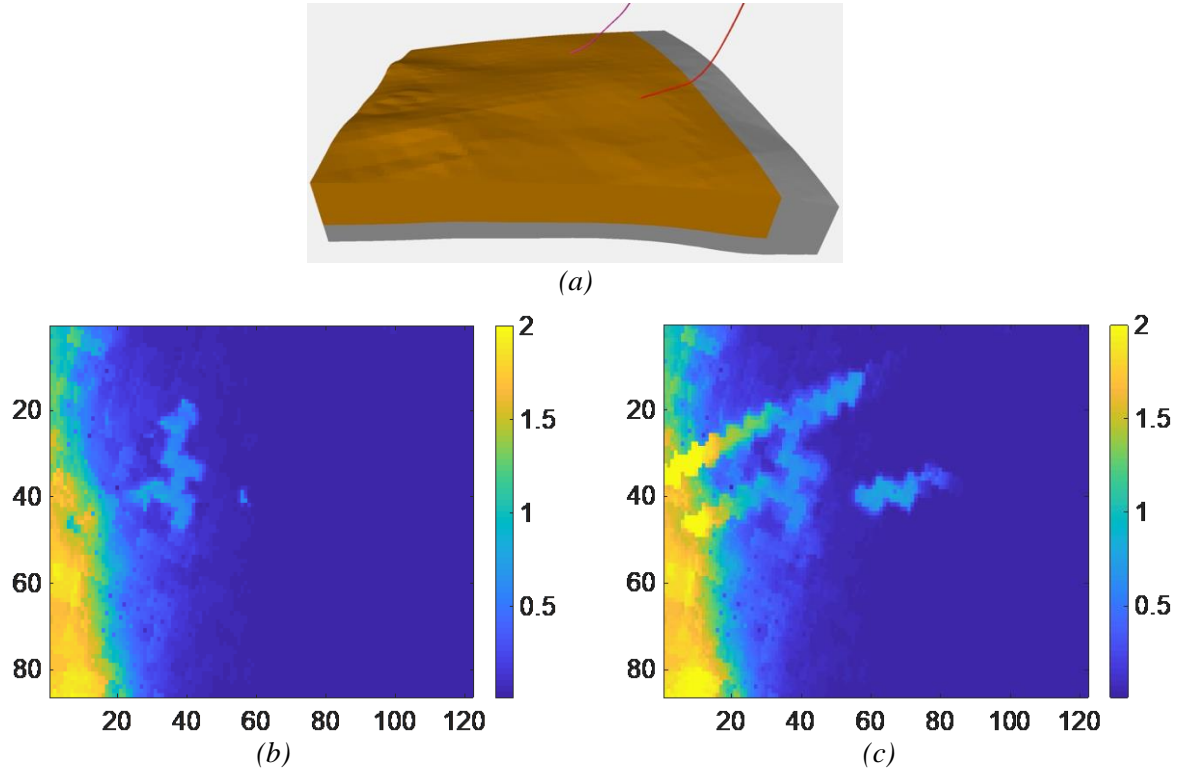
*(a)*



*(b)*            *(c)*

***Figure 3*** *Cross-well EM data for history matching: (a) subdomain (in brown) defines the valid volume of resistivity from which 2D resistivity maps are computed, (b) reciprocal of resistivity (i.e., conductivity) map at Year 1, (c) reciprocal of resistivity map at Year 7.*

**Parameterization and initial ensemble sampling**

The identified uncertain model variables for history matching include matrix porosity (MPORO), matrix permeability (in x- and z-directions, i.e., MPERMX and MPERMZ), fracture porosity (FPORO), fracture permeability (in x- and z-directions, i.e., FPERMX and FPERMZ), cementation exponent $m$ and saturation exponent $n$ in Archie's law. To model the prior uncertainty of reservoir matrix properties, facies modeling is implemented first to capture the geological heterogeneity with a multipoint-based geostatistical algorithm (Strebelle, 2012). Subsequently, conditioned on the generated realizations of geological facies, realizations of matrix porosity and permeability are generated with a sequential Gaussian simulation in which variogram models are estimated from well logs. Figure 4 shows two sample realizations of matrix porosity and permeability in Layer 1 of the simulation model.
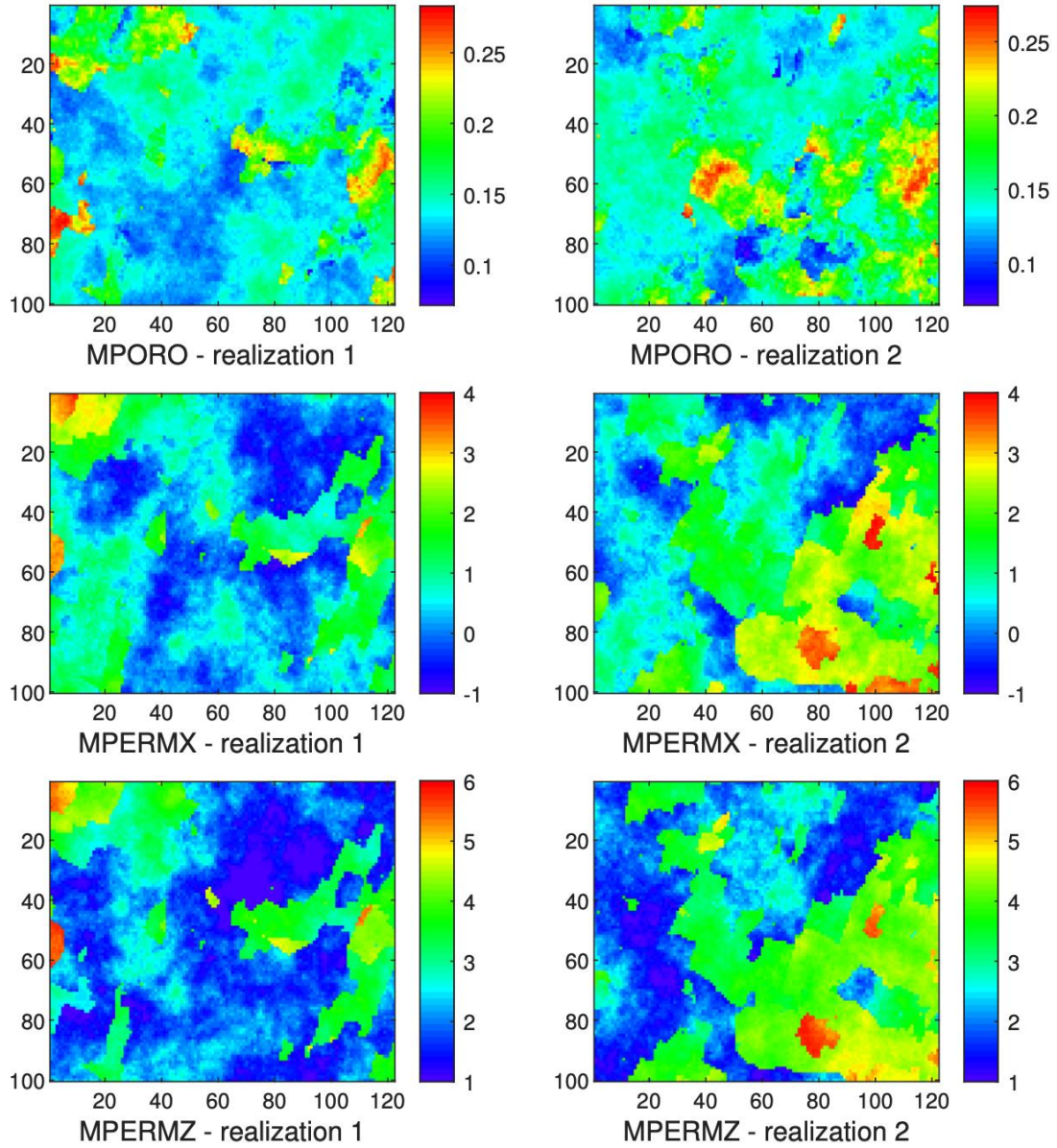
7

*Figure 4* *Two sample initial realizations in Layer 1 for reservoir matrix properties: MPORO, MPERMX and MPERMZ.*

A hybrid parameterization approach is applied to parameterize the uncertainty of multiscale fracture network. For large-scale structures, their location is assumed to be identified, for instance, from seismic data and well logs (Souche et al., 2012), but the porosity and permeability within the large-scale fractures are assumed to be uncertain. These properties are distributed uniformly and drawn from uniform distributions with the ranges of [0.01, 0.07] for FPORO[L], [500, 5000] mD for FPERMX[L], and [1, 5] mD for FPERMZ[L]. The corresponding large-scale fracture properties of the reference reservoir model take values of 0.04, 3669 mD, and 1.67 mD, respectively. For small-scale fractures, a truncated Gaussian simulation (TGS) method is used to capture their spatial distribution (Dowd et al., 2007; Yao et al., 2019). The location of small-scale fractures is represented by a Gaussian random field ($\mathcal{G}$), which is defined as an indicator (I) for the spatial distribution of the fractures,

$$I(x, y, z) = \begin{cases} 1 \text{ (fractured region), if } \mathcal{G}(x, y, z) > \tau \\ 0 \text{ (nonfractured region), if } \mathcal{G}(x, y, z) \leq \tau \end{cases}, \tag{5}$$

8

where $\tau$ is a threshold value and set to be 0.5 in the experiment. By conditioning the Gaussian random field to the observations, we can therefore update the location of the small-scale fractures accordingly. Figure 5 shows a couple of sample realizations of the distribution of small-scale fractures via TGS. The porosity and permeability within the small-scale fractures are distributed uniformly and sampled from uniform distributions with the ranges of [0.01, 0.04] for FPORO$^S$, [50, 1000] mD for FPERMX$^S$, and [1, 10] mD for FPERMZ$^S$. The corresponding small-scale fracture properties of the reference reservoir model take values of 0.02, 325 mD, and 3.5 mD, respectively. Archie's parameters $m$ and $n$ are sampled from uniform distributions as well with a range of [1.4, 2.4]. As a result, an ensemble of 100 realizations of the considered model variables is generated to represent the prior uncertainty in the model. The total number of model parameters considered in the experiment is over one million.
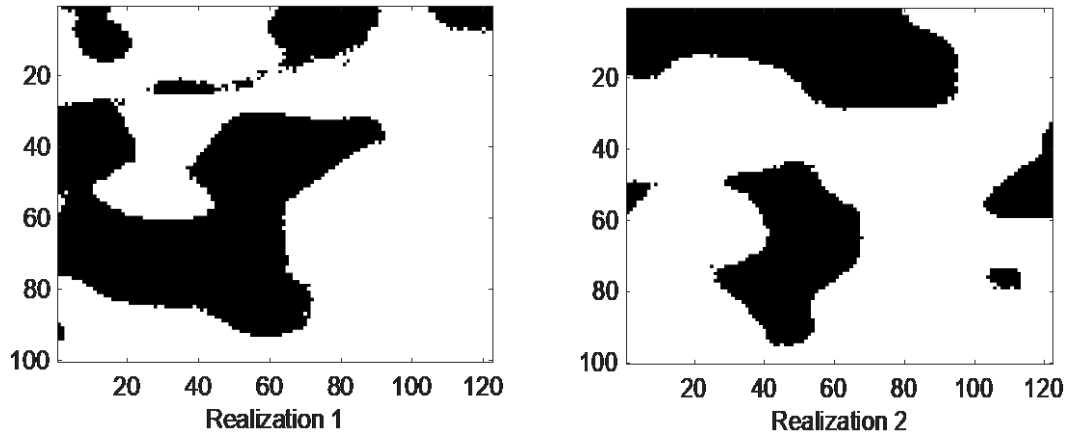


***Figure 5*** *Two sample initial realizations in Layer 1 for the distribution of small-scale fractures (in black).*

## Feature-oriented integration of resistivity maps

Although the number of EM data has been greatly reduced by the use of the 2D resistivity maps as shown in Figure 3, the compressed number of data is still big, over 10,000. Moreover, the magnitudes of individual grid blocks in the resistivity map from EM inversion often involve large uncertainty that is difficult to quantify. Therefore, to circumvent these difficulties resulted from the direct integration, we instead utilize the shape information of reproduced features in the resistivity maps by employing a distance parameterization (Zhang and Leeuwenburgh, 2017) combined with the ensemble assimilation methods.

For the resistivity map, the feature of interest is related to the shape of resistivity anomalies, which are induced by saturation changes and the inherent high resistivity contrast between oil and salt water. To extract associated features coherently from the resistivity maps, we adopt a simple image segmentation procedure involving spatial smoothing and thresholding. Figure 6 shows the extracted shapes (in red contours) from the smoothed reciprocals of resistivity maps with a threshold value of 0.1. The positions of these extracted contours will be then used as the observations for history matching.
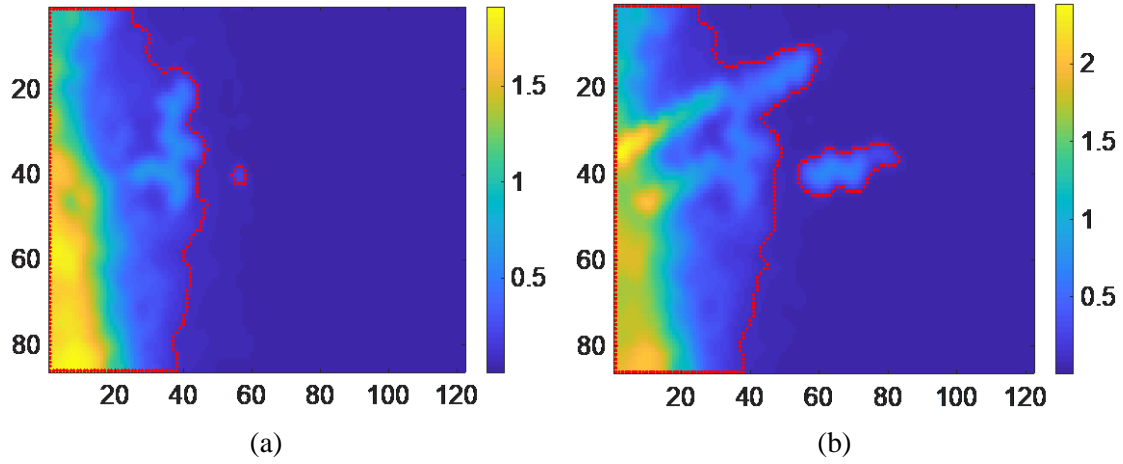
9

***Figure 6*** *Smoothed reciprocals of resistivity maps at Year 1 (a) and Year 7 (b) from which the contours (in red dots) of anomalies are extracted with a threshold value of 0.1 for history matching.*

To quantify the difference between 'observed' and simulated contours of resistivity anomalies, we select the scheme termed as LHDC (local Hausdorff distance based on contour) in Zhang and Leeuwenburgh (2017). Let matrices $\mathbf{I}_{obs}$ and $\mathbf{I}_{sim}$ denote the binary images (0 for the background and 1 for the contour) corresponding to the observed contour $\mathbf{c}_{obs}$ and the simulated contour $\mathbf{c}_{sim}$, respectively. In the LHDC, the difference between two contours is measured by,

$$\text{LHDC}(\mathbf{c}_{obs}, \mathbf{c}_{sim}) = \mathbf{I}_{obs} \circ \mathbf{D}_{sim} + \mathbf{I}_{sim} \circ \mathbf{D}_{obs}, \qquad (6)$$

where $\boldsymbol{D}_{obs}$ and $\boldsymbol{D}_{sim}$ are the corresponding distance maps for the contours $\boldsymbol{c}_{obs}$ and $\boldsymbol{c}_{sim}$, respectively. There exist readily available algorithms to compute these distance maps efficiently such as the fast marching methods (Gillberg et al., 2012; Zhang and Leeuwenburgh, 2016). The value at each location of a distance map measures the distance from this location to the nearest location on a contour in the binary image. Briefly speaking, the difference of the contours in the LHDC is quantified by the sum of two directed distance maps in complementary directions, $\boldsymbol{I}_{obs} \circ \boldsymbol{D}_{sim}$ (distance from $\boldsymbol{c}_{sim}$ to $\boldsymbol{c}_{obs}$) and $\boldsymbol{I}_{sim} \circ \boldsymbol{D}_{obs}$ (distance from $\boldsymbol{c}_{obs}$ to $\boldsymbol{c}_{sim}$). After applying the LHDC, the observed feature is converted to zero distance map, i.e., $\boldsymbol{d}_{obs} = LHDC(\boldsymbol{c}_{obs}, \boldsymbol{c}_{obs}) = \boldsymbol{0}$ and the simulated feature is converted to the dissimilarity distance map, i.e., $\boldsymbol{d}_{sim,j} = LHDC(\boldsymbol{c}_{obs}, \boldsymbol{c}_{sim,j})$. The reparametrized distance data are then assimilated by the LM-EnRML. Uncorrelated distance-measurement errors are assumed with a standard deviation of one grid block length. A more complete description of the distance parameterization method can be found in Zhang and Leeuwenburgh (2017).

**Kalman gain localization**

It is usually necessary to apply some type of regularization when the ensemble methods are used for history matching. The regularization is implemented basically for two reasons. The first is to reduce the impact of spurious correlations that may result in over-reduction of ensemble variability or even collapse, and the second is to increase the number of degrees of freedom in order to fit the data when its number is much larger than the ensemble size. In this study, we use an adaptive Kalman gain localization method introduced by Zhang and Oliver (2010). This localization method utilizes bootstrap sampling to assess the confidence level of each element in the Kalman gain matrix, so that the real and the spurious correlations can be discriminated. One advantage of the bootstrap-based localization over the distance-based localization is its easy adaption to the cases involving multiple types of model variables, in which the selection of distance functions can be complicated or even intractable for some model variables (like the Archie's parameters considered here). As will be described below, the bootstrap-based screening also allows the flexibility to implement the localization in the reduced data subspace, which expedites the computation significantly when the model and data dimensions are very

10

large. In the standard implementation, the localized Kalman gain is obtained by multiplying the original Kalman gain with a localization matrix $\mathbf{L}$

$$\mathbf{K}^{loc} = \mathbf{L} \circ \overbrace{\left\{ \Delta\mathbf{M}^{\ell}\Delta\mathbf{D}^{\ell\mathrm{T}}\left[(1+\lambda_{\ell})\mathbf{I}_{\mathrm{N_d}} + \Delta\mathbf{D}^{\ell}\Delta\mathbf{D}^{\ell\mathrm{T}}\right]^{-1} \right\}}^{\text{Kalman gain } \mathbf{K}}, \tag{7}$$

where the operator $\circ$ represents the element-wise multiplication. Each element of $\mathbf{L}_{ij}$ in the localization matrix is computed as

$$\mathbf{L}_{ij} = \left[1 + \mathbf{R}_{ij}^2\left(1 + \frac{1}{\gamma^2}\right)\right]^{-1}, \text{wherein } \mathbf{R}_{ij}^2 = \frac{\sum_{l=1}^{\mathrm{N_b}}\left(\mathbf{K}_{ij}^l - \mathbf{K}_{ij}\right)^2}{\mathrm{N_b} \cdot \mathbf{K}_{ij}^2}, \tag{8}$$

for $i = 1, 2, \dots, \mathrm{N}_m, j = 1, 2, \dots, \mathrm{N}_d$. The term $\mathbf{K}_{ij}^l$ represents an element in the $l$th bootstrapped sample of the Kalman gain matrix, and $\mathrm{N_b}$ denotes the number of bootstrapped samples. More implementational detail about the bootstrap sampling of the Kalman gain is given in Appendix B. Our experience from the conducted experiments indicates that setting $\mathrm{N_b} = 50$ is sufficient to ensure the screening performance of the bootstrap-based localization.

The computational cost of the bootstrap-based localization depends on the dimensions of the Kalman gain matrix. It becomes expensive when the number of data is large. To improve the computational efficiency, we first project the data onto its subspace and then implement the bootstrap-based Kalman gain localization in the projected data space. The projection is achieved via a truncated singular value decomposition of $\Delta\mathbf{D}^{\ell}$ as

$$\Delta\mathbf{D}^{\ell} = \mathbf{U}_p^{\ell}\,\mathbf{W}_p^{\ell}\mathbf{V}_p^{\ell\mathrm{T}}, \tag{9}$$

where $p$ is the number of singular values retained after truncation ($p \leq \mathrm{N_e} - 1$, 99% energy retained in this study) and the dimensions for the matrices $\mathbf{U}_p^{\ell}$, $\mathbf{W}_p^{\ell}$, and $\mathbf{V}_p^{\ell}$ are $\mathrm{N_d} \times p$, $p \times p$, and $\mathrm{N_e} \times p$ respectively. Taking Eq. 9 back in Eq. 1, the updating formula becomes

$$\delta\mathbf{m}_i^{\ell} = \underbrace{\Delta\mathbf{M}^{\ell}\left(\mathbf{U}_p^{\ell\mathrm{T}}\Delta\mathbf{D}^{\ell}\right)^{\mathrm{T}}\left[(1+\lambda_{\ell})\mathbf{I}_p + \mathbf{W}_p^{\ell 2}\right]^{-1}}_{\text{effective Kalman gain } \mathbf{K}^{eff}}\underbrace{\mathbf{U}_p^{\ell\mathrm{T}}\mathbf{C}_{\mathrm{D}}^{-\frac{1}{2}}\left[\mathbf{d}_{\mathrm{obs},i} - \mathbf{g}\left(\mathbf{m}_i^{\ell}\right)\right]}_{\text{effective innovation}}. \tag{10}$$

This reformulation was first introduced by Chen and Oliver (2017). In Eq. 10, the original Kalman gain $\mathbf{K}$ of dimensions $\mathrm{N_m} \times \mathrm{N_d}$ is replaced with the effective Kalman gain $\mathbf{K}^{eff}$ of dimensions $\mathrm{N_m} \times p$. In the case of $p \ll \mathrm{N_d}$, a significant reduction of the computational cost can therefore be achieved when implementing the bootstrap-based localization in the data subspace spanned by the columns of $\mathbf{U}_p^{\ell\mathrm{T}}$, i.e.,

$$\mathbf{K}^{eff,loc} = \mathbf{L} \circ \left\{ \Delta\mathbf{M}^{\ell}\left(\mathbf{U}_p^{\ell\mathrm{T}}\Delta\mathbf{D}^{\ell}\right)^{\mathrm{T}}\left[(1+\lambda_{\ell})\mathbf{I}_p + \mathbf{W}_p^{\ell 2}\right]^{-1} \right\}. \tag{11}$$

In Eq. 8, the degree of screening to spurious correlations is controlled by the weighting factor $\gamma$, which also precludes the estimate of $\mathbf{L}$ from taking negative values. The value of $\mathbf{R}_{ij}^2$ indicates the reliability of the correlations present in the matrix of Kalman gain. Obviously, smaller values of $\mathbf{R}_{ij}^2$ (or equivalently larger values of $\mathbf{L}_{ij}$) will impose less screening on the corresponding elements in the Kalman gain, therefore indicating more reliable correlations of the related model variable with the data, and vice versa. Intuitively, we can penalize unreliable correlations (large $\mathbf{R}_{ij}^2$) in the Kalman gain by decreasing the value of $\gamma$, so that the confidence factor $\mathbf{L}_{ij}$ gets smaller value close to 0. By doing so, however, it will also slow down the convergence rate resulting in more iterations required. In Zhang and Oliver (2010), a single value of $\gamma$ was used. However, one drawback of using a single value of $\gamma$ is that it is not straightforward to select a suitable value of $\gamma$ to balance the tradeoff between the reduction

11

of spurious correlations and the computational cost. To overcome this difficulty, we propose to adapt the value of $\gamma$ to each confidence factor $\mathbf{L}_{ij}$ in a heuristic fashion by using a Gaussian-type taper function as

$$\gamma_{ij}^2 = \alpha \exp\left(-\frac{\mathbf{R}_{ij}^2}{\beta^2}\right), \tag{12}$$

where $\alpha$ defines the maximum value of $\gamma_{ij}^2$ (i.e., $\mathbf{R}_{ij}^2 = 0$) and $\beta$ controls the decaying rate of $\gamma_{ij}^2$ with increasing variance $\mathbf{R}_{ij}^2$. Figure 7 shows how the value of $\gamma_{ij}^2$ changes when $\alpha$ and $\beta$ take different values. The main idea of the adaptive tapering for the weighting factor $\gamma$ is to apply less screening on the more reliable elements (small $\mathbf{R}_{ij}^2$) while still reducing the effect of the unreliable elements (large $\mathbf{R}_{ij}^2$) in the Kalman gain. In this study, $\alpha = 0.6$ and $\beta = 0.3$ (red solid line in Figure 7) are selected based on trial and error. Our experience indicates that selecting $\alpha \in [0.5, 1]$ and $\beta \in [0.25, 0.35]$ usually gives relatively robust performance.
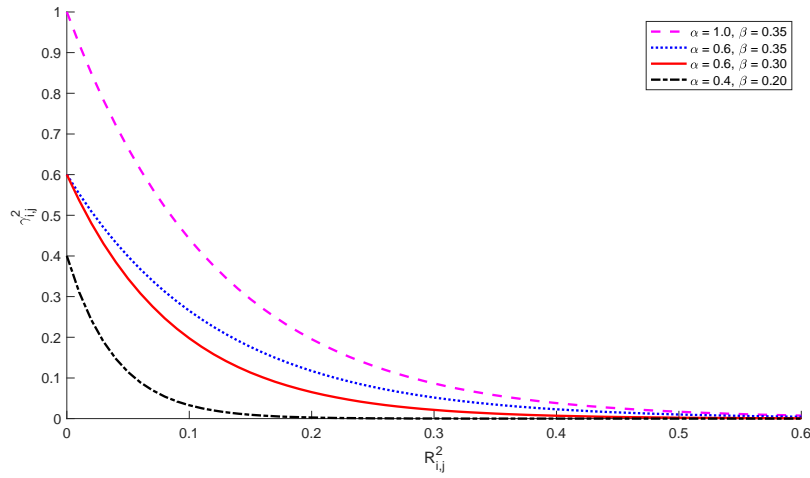


**Figure 7** *Gaussian-type taper function with different settings of input parameters, among which $\alpha = 0.6$ and $\beta = 0.3$ (red solid line) are selected for the experiment.*

**Results and discussions**

A pair of comparative experiments with separate use of production and EM data were first conducted to examine the information contained in each type of data for the characterization of uncertain model parameters. Figure 8 shows the reduction of production data mismatch (in log-transformed scale) and the distribution of RMSEs of updated ensemble members of model parameters along with iterations. The RMSE is given by

$$\text{RMSE} = \left[\sum_{j=1}^{N_m}\left(\mathbf{m}_{i,j} - \mathbf{m}_{t,j}\right)^2 / N_m\right]^{1/2}, \tag{13}$$

where i denotes realization number, j denotes element index, and t represents reference model property. In general, the smaller the RMSE is, the closer the corresponding updated model parameters get to the reference ones. In the case of only production data assimilated, the main improvement in the model update comes from the horizontal permeability for both large-scale and small-scale fractures (FPERMX), while the RMSEs of the other model parameters are hardly reduced. This behavior is anticipated because of the high-permeable flow corridors formed by the fracture network, which plays a dominant role in the production of associated wells. The result also indicates that for fractured carbonate reservoirs, due to the involved geological complexity and large uncertainty, it is necessary to

12

assimilate more types of available data to complement the limited information content of production data for better characterization of reservoir properties.
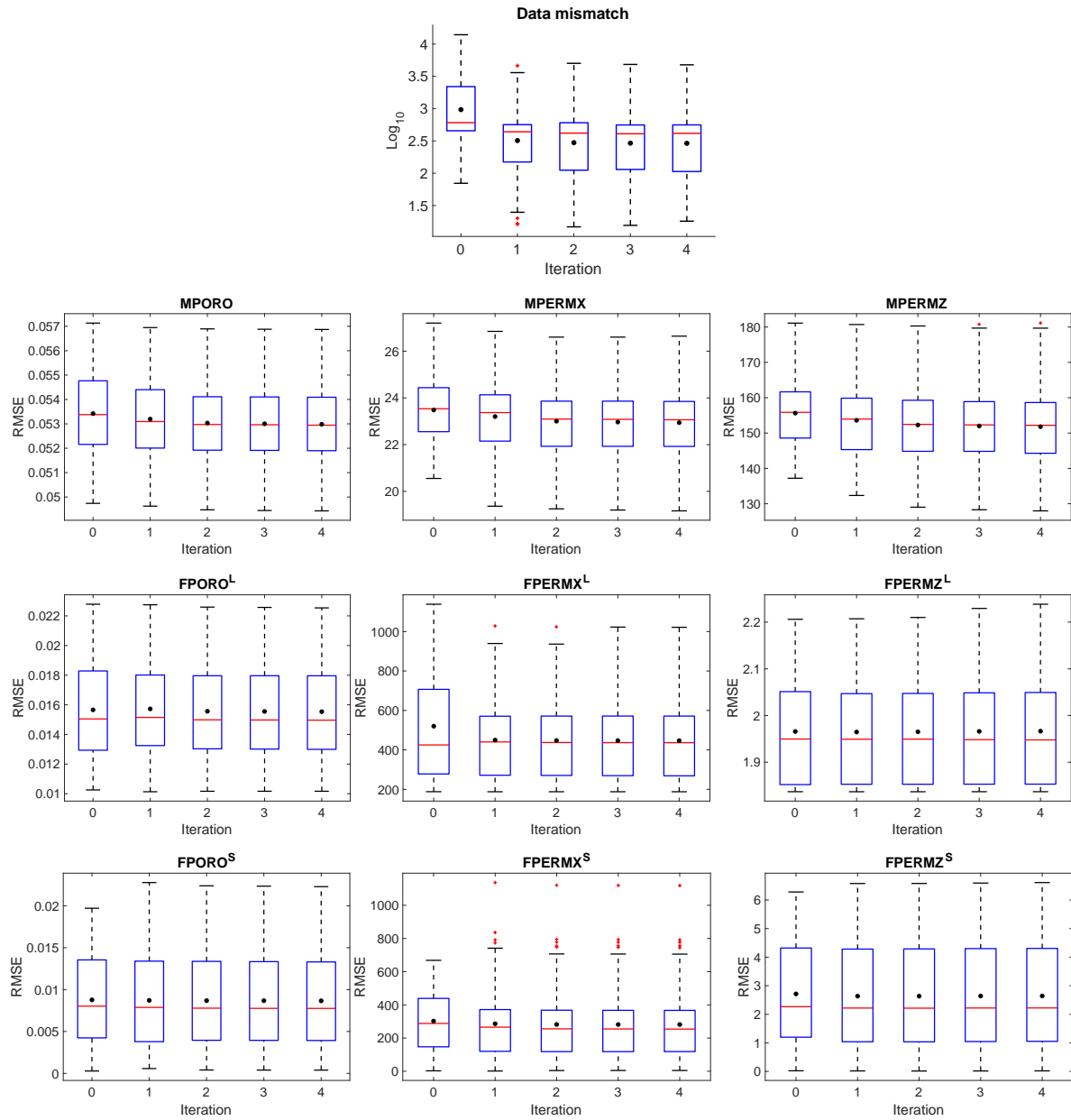


***Figure 8*** *Boxplots of data mismatch (in log-transformed scale) and the RMSEs of model parameters during the iteration using production data only. The bounds of the box are 25% and 75% quantiles, the whiskers are the extremes, the line in the box is the median, the dot is mean, and the pluses are outliers.*

Figure 9 shows the result of data mismatch and the RMSEs of the updated ensemble of model parameters during the iteration, when only EM data from Year 1 are history matched. Compared with the previous case when only production data are assimilated, the overall performance on the model improvement is significant. There is a pronounced and consistent reduction of the RMSE for most of the updated model variables along with iterations. The result also illustrates the rich information content of the EM data and the efficacy of the feature-based integration approach that captures the essential information contained in the original data. For easy comparison, Table 2 summarizes the mean and standard deviation of the RMSEs of the final ensembles of model variables for all considered cases.
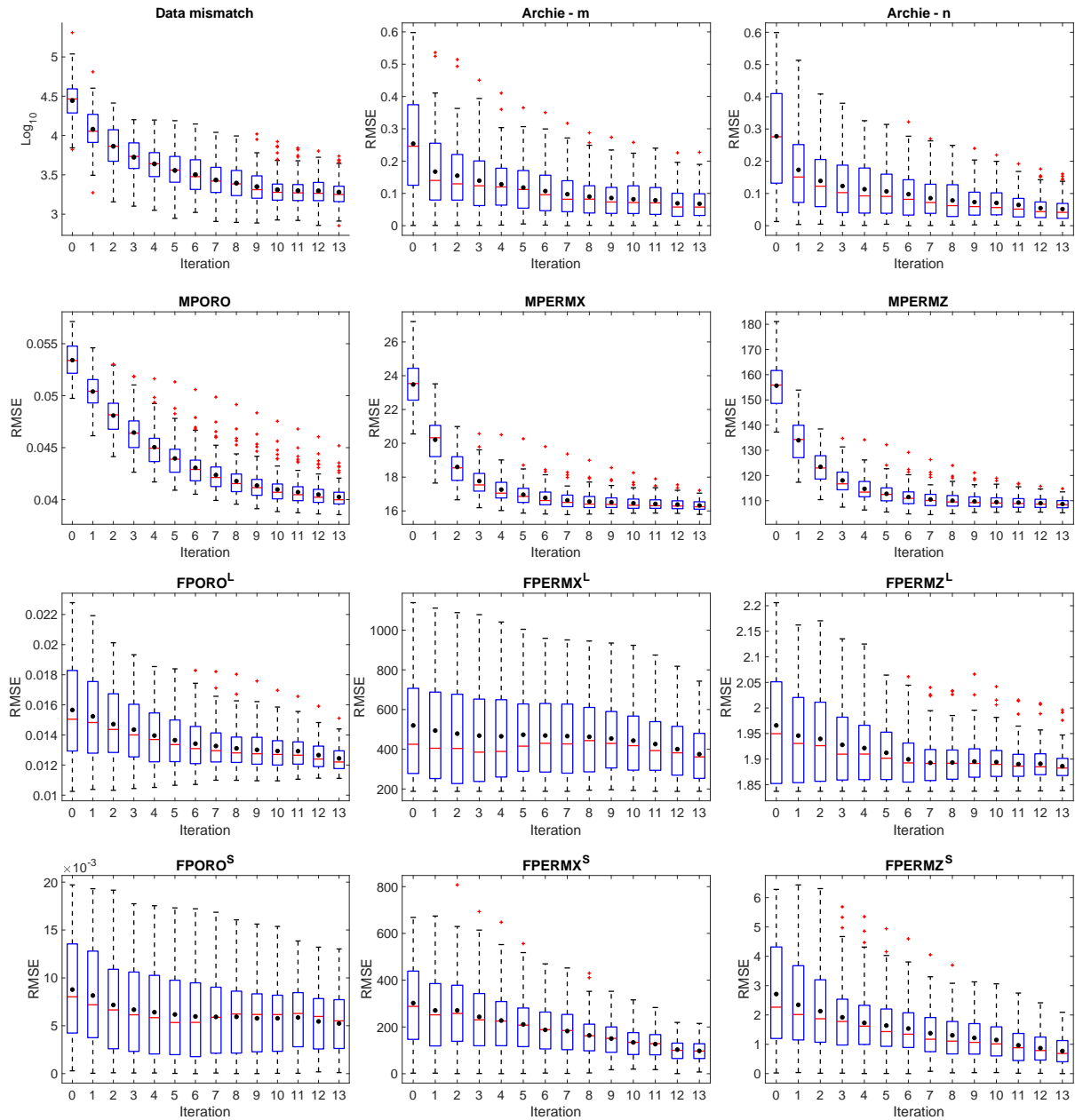
13

***Figure 9*** *Boxplots of data mismatch (in log-transformed scale) and the RMSEs of model parameters during the iteration using EM data only (Year 1). The bounds of the box are 25% and 75% quantiles, the whiskers are the extremes, the line in the box is the median, the dot is mean, and the pluses are outliers.*

***Table 2*** *Statistical summary (mean ± standard deviation) of the RMSEs of the final ensembles of model variables for all cases.*

|  | Archie - m | Archie - n | MPORO | MPERMX | MPERMZ | FPORO$^L$ |
|---|---|---|---|---|---|---|
| Production only | – | – | 0.053 ± 0.002 | 22.94 ± 1.55 | 151.8 ± 10.6 | 0.016 ± 0.003 |
| EM only | 0.068 ± 0.049 | 0.052 ± 0.041 | 0.042 ± 0.001 | 16.32 ± 0.31 | 108.7 ± 2.1 | 0.013 ± 0.001 |
| Joint | 0.049 ± 0.043 | 0.048 ± 0.041 | 0.041 ± 0.001 | 16.30 ± 0.33 | 110.5 ± 2.2 | 0.012 ± 0.001 |
|  | FPERMX$^L$ | FPERMZ$^L$ | FPORO$^S$ | FPERMX$^S$ | FPERMZ$^S$ | |
| Production only | 447.1 ± 202.3 | 1.97 ± 0.11 | 0.009 ± 0.006 | 281.2 ± 210.4 | 2.64 ± 1.86 | |
| EM only | 375.1 ± 139.8 | 1.89 ± 0.03 | 0.006 ± 0.003 | 97.8 ± 47.7 | 0.77 ± 0.52 | |
| Joint | 390.6 ± 91.6 | 1.88 ± 0.03 | 0.005 ± 0.003 | 114.1 ± 49.2 | 0.81 ± 0.64 | |

14

As the above comparative experiments indicate, the EM data provide abundant additional information that complements the production data with the potential to improve the characterization of the considered model parameters. As a result, in the last experiment, both production and EM data (including Year 1 and Year 7 as in Figure 6) are assimilated using the feature-oriented ensemble history matching workflow.

Figure 10 compares the distributions of the interpreted resistivity fronts (contours) from the forward simulation of the initial model ensemble and the final updated model ensemble after the joint production-EM history matching. Even though the initial distributions of resistivity fronts display large variation, the final distributions of resistivity fronts show a reasonable match to the reference ones. Meanwhile, a significant model improvement is achieved for updated model parameters after the joint history matching as shown in Figure 11.
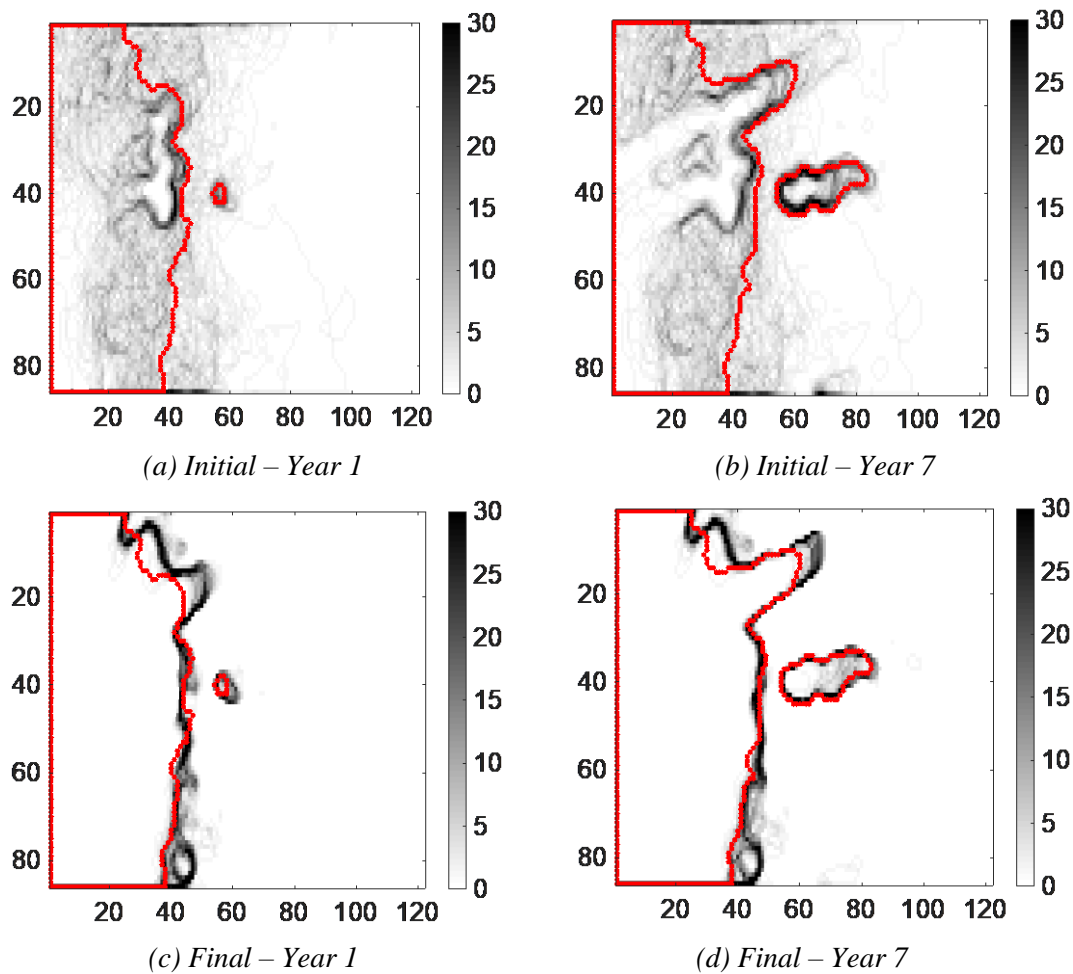


*(a) Initial – Year 1*

*(b) Initial – Year 7*

*(c) Final – Year 1*

*(d) Final – Year 7*

**Figure 10** *Distributions of interpreted resistivity fronts or contours at two EM survey times before (a, b) and after (c, d) history matching. The grayscale indicates the count of occurrence of resistivity front at a location. The upper color map limit is mapped from 100 (the ensemble size) to 30 for better visibility.*
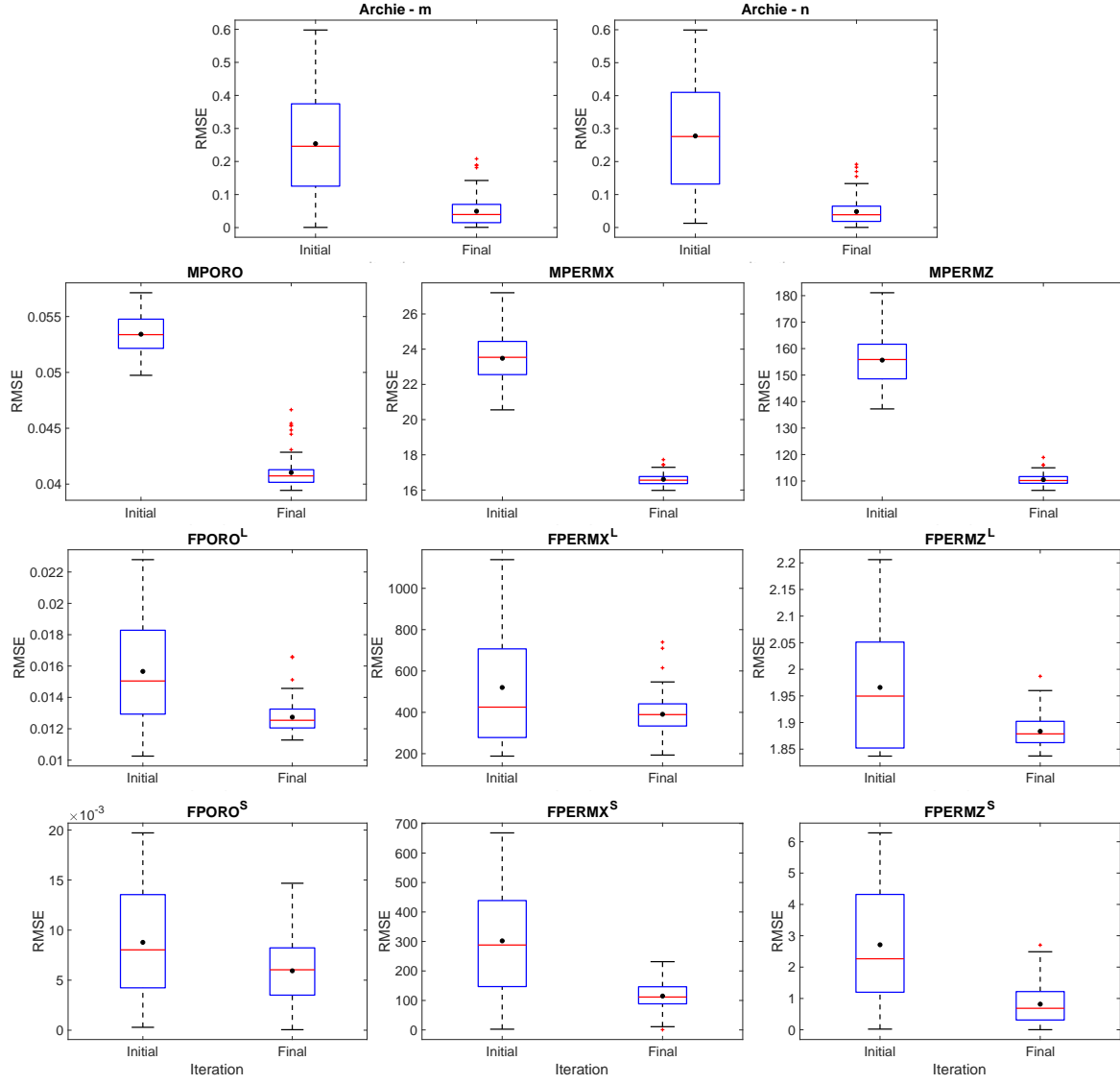
15

***Figure 11*** *Comparison of the RMSEs of model parameters before and after history matching. The bounds of the box are 25% and 75% quantiles, the whiskers are the extremes, the line in the box is the median, the dot is mean, and the pluses are outliers.*

Figure 12 displays the probability maps of the small-scale fractures in some layers before and after the history matching. The fracture distribution is obtained by truncating the Gaussian random fields from the initial and final updated ensembles. The probability map of the fractures is calculated by

$$P_{x,y,z}^F = \frac{\sum_{i=1}^{N_e} \mathbf{1}[\mathcal{G}(x,y,z)]}{N_e}, \tag{14}$$

where

$$\mathbf{1}[\mathcal{G}(x,y,z)] = \begin{cases} 1, & \text{if } \mathcal{G}(x,y,z) > 0.5 \\ 0, & \text{if } \mathcal{G}(x,y,z) \le 0.5 \end{cases}. \tag{15}$$

It is clear to see from the initial probability maps in Figure 12 that the small-scale fractures occur basically uniformly across the reservoir for the initial ensemble. After history matching, the updated probability maps indicate that the final ensemble of updated model parameters captures the fracture distribution in the reference reservoir to a certain degree. For instance, the fracture probability in the central area of Layer 7 is reduced while it is retained in Layer 11, which is consistent with the reference

16

model. However, due to the limited information and intricate geological complexities, the characterization of the small-scale fractures is still poor in general.
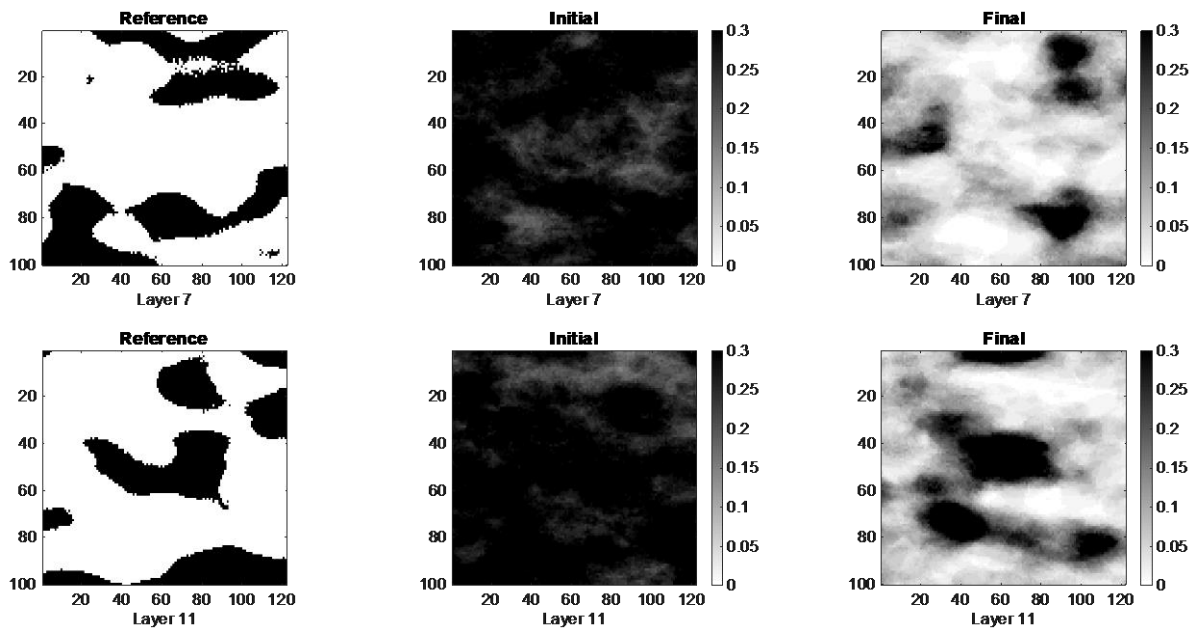


*Figure 12* *The distribution of small-scale fractures for the reference reservoir model (left), and the probability maps of the fractured area for the initial ensemble (middle) and the final updated ensemble (right). The upper color map limit is truncated for better visibility.*

Due to the inherent complexity in the characterization of fractured carbonate reservoir models, some simplification made in this study may be worth of future investigation for further improvement. Firstly, deterministic modeling of large-scale fracture network has been used in the experiment. However, to better quantify the uncertainty of fracture distribution and properties, an integrated stochastic modeling procedure of the fracture network might be more appropriate, for instance, through a DFN model (Nejadi et al., 2017, Maucec et al., 2020). Extension of the developed workflow with the integrated fracture modeling seems straightforward. Secondly, the uncertainty in the rock physics model is represented by Archie's parameters which are assumed to be uniform in the experiment. However, as pointed out by Hamada (2010), Archie's parameters can be heterogeneous and quite uncertain for some formations, especially carbonate rocks. Refining the parameterization and estimation of these parameters is therefore expected to enhance the performance of the developed workflow in characterizing complex reservoirs.

**Conclusions**

We showcased the application of a feature-oriented ensemble-based history matching workflow to a complex fractured carbonate model using production and cross-well EM data. The developed workflow expedites the conditioning of complex reservoir models to high-dimensional geophysical data, by combining a feature-based integration approach with a data subspace localization method. Instead of the direct integration of the inverted EM resistivity data, which are often in high dimensions and noisy in amplitudes, the workflow assimilates the contour information interpreted from the EM resistivity field using an iterative ensemble smoother together with a distance parameterization. A modified bootstrap-based localization is proposed to regularize the iterative model update, in order to reduce the effect of sampling errors and increase the number of degrees of freedom. Due to the large dimensions of both model and data, the localization is implemented in a projected low-dimensional data subspace to improve the computational efficiency.

A comparative case study was implemented to examine the added value of deep EM data in improving the characterization of fractured carbonate reservoirs using the developed workflow. The experimental results demonstrated the efficacy of the developed feature-oriented workflow for the

17

conditioning of realistic reservoir models to high-dimensional geophysical data. The comparative case study also illustrated the great potential of deep EM data for enhancing the characterization of complex carbonate reservoirs.

## References

Aanonsen, S.I., Nævdal, G., Oliver, D.S., Reynolds, A.C., Vallès, B., 2009. The Ensemble Kalman Filter in Reservoir Engineering – a Review. SPE J. 14, 393–412. https://doi.org/10.2118/117274-PA

Abadpour, A., Adejare, M., Chugunova, T., Mathieu, H., Haller, N., 2018. Integrated geo-modeling and ensemble history matching of complex fractured carbonate and deep offshore turbidite fields, generation of several geologically coherent solutions using ensemble methods, in: Abu Dhabi International Petroleum Exhibition & Conference.

Al-Ali, Z., H. Al-Buali, M., AlRuwaili, S., Ma, S.M., Marsala, A.F., Hulme, C., Wilt, M., 2009. Looking deep into the reservoir. Oilf. Rev. 21, 38–47.

Archie, G.E., 1942. The electrical resistivity log as an aid in determining some reservoir characteristics. Trans. AIME 146, 54–62. https://doi.org/10.2118/942054-G

Chen, Y., Oliver, D.S., 2017. Localization and regularization for iterative ensemble smoothers. Comput. Geosci. 21, 13–30. https://doi.org/10.1007/s10596-016-9599-7

Chen, Y., Oliver, D.S., 2014. History matching of the norne full-field model with an iterative ensemble smoother. SPE Reserv. Eval. Eng. 17, 244–256.

Chen, Y., Oliver, D.S., 2013. Levenberg-Marquardt forms of the iterative ensemble smoother for efficient history matching and uncertainty quantification. Comput. Geosci. 17, 689–703. https://doi.org/10.1007/s10596-013-9351-5

Dovera, L., Della Rossa, E., 2011. Multimodal ensemble Kalman filtering using Gaussian mixture models. Comput. Geosci. 15, 307–323. https://doi.org/10.1007/s10596-010-9205-3

Dowd, P.A., Xu, C., Mardia, K. V., Fowell, R.J., 2007. A comparison of methods for the stochastic simulation of rock fractures. Math. Geol. 39, 697–714. https://doi.org/10.1007/s11004-007-9116-6

Dresser, A., 1982. Well logging and interpretation techniques. The course for home study. Dresser Atlas.

Emerick, A.A., Reynolds, A.C., 2013. Ensemble smoother with multiple data assimilation. Comput. Geosci. 55, 3–15. https://doi.org/10.1016/j.cageo.2012.03.011

Gillberg, T., Hjelle, Ø., Magnus, A., 2012. Accuracy and efficiency of stencils for the eikonal equation in earth modelling 933–952. https://doi.org/10.1007/s10596-012-9296-0

Hamada, G.M., 2010. Analysis of archie's parameters determination techniques. Pet. Sci. Technol. 28, 79–92. https://doi.org/10.1080/10916460802706463

Hoteit, I., Luo, X., Pham, D.-T., 2012. Particle Kalman filtering: a nonlinear Bayesian framework for ensemble Kalman filters. Mon. Weather Rev. 140, 528–542. https://doi.org/10.1175/2011MWR3640.1

Jung, S., Lee, K., Park, C., Choe, J., 2018. Ensemble-based data assimilation in reservoir characterization: A review. Energies 11, 445. https://doi.org/10.3390/en11020445

Katterbauer, K., Hoteit, I., Sun, S., 2016. Synergizing crosswell seismic and electromagnetic techniques for enhancing reservoir characterization. SPE J. 21, 909–927. https://doi.org/10.2118/174559-pa

Leeuwenburgh, O., Arts, R., 2014. Distance parameterization for efficient seismic history matching with the ensemble Kalman Filter. Comput. Geosci. 18, 535–548. https://doi.org/10.1007/s10596-014-9434-y

Liang, L., Abubakar, A., Habashy, T.M., 2016. Reservoir property mapping and monitoring from joint inversion of time-lapse seismic, electromagnetic, and production data. Geophysics 81, 73–84. https://doi.org/10.1190/geo2015-0620.1

Liu, B., Ait-El-Fquih, B., Hoteit, I., 2016. Efficient kernel-based ensemble Gaussian mixture filtering. Mon. Weather Rev. 144, 781–800. https://doi.org/10.1175/MWR-D-14-00292.1

Lorentzen, R.J., Flornes, K.M., Nævdal, G., 2012. History matching channelized reservoirs using the ensemble kalman filter. SPE J. 17, 137–151. https://doi.org/10.2118/143188-PA

Lorentzen, R.J., Luo, X., Bhakta, T., Valestrand, R., 2019. History matching the full Norne field model using seismic and production data. SPE J. 1–16. https://doi.org/10.2118/194205-pa

18

Lu, L., Zhang, D., 2015. Assisted history matching for fractured reservoirs by use of hough-transform-based parameterization. SPE J. 20, 942–961. https://doi.org/10.2118/176024-pa

Luo, X., Bhakta, T., Jakobsen, M., Nævdal, G., 2017. An ensemble 4D-seismic history-matching framework with sparse representation based on wavelet multiresolution analysis. SPE J. 22, 985–1010. https://doi.org/10.2118/180025-PA

Luo, X., Bhakta, T., Nævdal, G., 2018. Correlation-based adaptive localization with applications to ensemble-based 4D-seismic history matching. SPE J. 23, 396–427. https://doi.org/10.2118/185936-PA

Luo, X., Stordal, A.S., Lorentzen, R.J., Nævdal, G., 2015. Iterative ensemble smoother as an approximate solution to a regularized minimum-average-cost problem : theory and applications. SPE J. 20, 962–982. https://doi.org/10.1086/309714

Marsala, A.F., Lyngra, S., Ma, S., Alsaif, S., 2017. Workflow to integrate geophysical deep EM and reservoir simulation for interwell saturation mapping, in: 79th EAGE Conference and Exhibition 2017 - Workshops. https://doi.org/10.3997/2214-4609.201701781

Marsala, A.F., Ruwaili, S., Ma, S.M., Ali, Z., Buali, M., Crary, S., Wilt, M., 2008. Crosswell electromagnetic tomography: From resistivity mapping to interwell fluid distribution, in: International Petroleum Technology Conference, IPTC 2008. pp. 1078–1083. https://doi.org/10.2523/iptc-12229-ms

Maucec, M., Zhang, S., Camargo, O.M., Olukoko, O., 2020. New approach to history matching of simulation models with discrete fracture networks, in: International Petroleum Technology Conference 2020, IPTC 2020. https://doi.org/10.2523/iptc-19962-ms

Nejadi, S., Trivedi, J.J., Leung, J., 2017. History matching and uncertainty quantification of discrete fracture network models in fractured reservoirs. J. Pet. Sci. Eng. 152, 21–32. https://doi.org/10.1016/j.petrol.2017.01.048

Obidegwu, D., Chassagne, R., MacBeth, C., 2017. Seismic assisted history matching using binary maps. J. Nat. Gas Sci. Eng. 42, 69–84. https://doi.org/10.1016/j.jngse.2017.03.001

Oliver, D.S., Alfonzo, M., 2018. Calibration of imperfect models to biased observations. Comput. Geosci. 22, 145–161. https://doi.org/10.1007/s10596-017-9678-4

Oliver, D.S., Chen, Y., 2011. Recent progress on reservoir history matching: A review. Comput. Geosci. 15, 185–221. https://doi.org/10.1007/s10596-010-9194-2

Soares, R.V., Luo, X., Evensen, G., Bhakta, T., 2021. Handling big models and big data sets in history-matching problems through an adaptive Local analysis scheme. SPE J. 26, 973–992. https://doi.org/10.2118/204221-pa

Soares, R. V., Luo, X., Evensen, G., Bhakta, T., 2020. 4D seismic history matching: Assessing the use of a dictionary learning based sparse representation method. J. Pet. Sci. Eng. 195, 107763. https://doi.org/10.1016/j.petrol.2020.107763

Souche, L., Astratti, D., Aarre, V., Clerc, N., Clark, A., Al Dayyni, T.N.A., Mahmoud, S.L., 2012. A dual representation of multiscale fracture network modelling: Application to a giant UAE carbonate field. First Break 30, 43–52. https://doi.org/10.3997/136S-2397.2012004

Strebelle, S., 2012. Multiple-Point Geostatistics : from Theory to Practice, in: Ninth International Geostatistics Congress. Springer, Oslo, Norway. pp. 11--15.

Sun, A.Y., 2011. Identification of geologic fault network geometry by using a grid-based ensemble Kalman filter. J. Hazardous, Toxic, Radioact. Waste 15, 228–233. https://doi.org/10.1061/(ASCE)HZ.1944-8376.0000072

Wilt, M.J., Alumbaugh, D.L., Morrison, H.F., Becker, A., Lee, K.H., Deszcz-Pan, M., 1995. Crosswell electromagnetic tomography: System design considerations and field results. Geophysics 60, 871–885. https://doi.org/10.1190/1.1443823

Yao, M., Chang, H., Li, X., Zhang, D., 2019. An integrated approach for history matching of multiscale-fracture reservoirs. SPE J. 24, 1508–1525. https://doi.org/10.2118/195589-PA

Zhang, K., Zhang, J., Ma, X., Yao, C., Zhang, L., Yang, Y., Wang, J., Yao, J., Zhao, H., 2021. History matching of naturally fractured reservoirs using a deep sparse autoencoder. SPE J. 1–22. https://doi.org/10.2118/205340-pa

Zhang, Y., Hoteit, I., 2021. Feature-oriented joint time-lapse seismic and electromagnetic history matching using ensemble methods. SPE J. 26, 1341–1365. https://doi.org/https://doi.org/10.2118/203847-PA

Zhang, Y., Leeuwenburgh, O., 2017. Image-oriented distance parameterization for ensemble-based seismic history matching. Comput. Geosci. 21, 713–731. https://doi.org/10.1007/s10596-017-9652-1

Zhang, Y., Leeuwenburgh, O., 2016. Ensemble-based seismic history matching with distance parameterization for complex grids, in: ECMOR XV - 15th European Conference on the Mathematics of Oil Recovery. https://doi.org/10.3997/2214-4609.201601815

Zhang, Y., Oliver, D.S., 2010. Improving the ensemble estimate of the Kalman gain by bootstrap sampling. Math. Geosci. 42, 327–345. https://doi.org/10.1007/s11004-010-9267-8

Zhang, Y., Oliver, D.S., Chen, Y., Skaug, H.J., 2014. Data assimilation by use of the iterative ensemble smoother for 2D facies models. SPE J. 20, 169–185. https://doi.org/10.2118/170248-PA

Zhang, Y., Vossepoel, F.C., Hoteit, I., 2020. Efficient assimilation of crosswell electromagnetic data using an ensemble-based history-matching framework. SPE J. 25, 119–138. https://doi.org/10.2118/193808-PA

## Appendix A. Tuning strategy of LM-EnRML

Regarding the tuning strategy for $\lambda$, we follow a heuristic rule that initializes $\lambda$ with a proper large value and gradually reduces it during the iteration. The rationale behind it is that a larger value of $\lambda$ brings the search direction closer to the steepest descent direction with a smaller step size, which is beneficial to stabilizing the model update as the initial data mismatch is often very large. On the other hand, reducing the value of $\lambda$ makes the algorithm closer to the Gauss–Newton algorithm, which may accelerate the convergence rate as the ongoing iteration approaches to the optimum solution. Specifically, the tunning strategy includes:

(i) The starting value of $\lambda_0$ is prescribed as the same order of magnitude as $\sum_{j=1}^{N_e} S_d(\mathbf{m}_j^0)/(2N_d)$, in which the data mismatch $S_d$ is defined by

$$S_d(\mathbf{m}_j) = \left[\mathbf{d}_{obs} - \mathbf{g}(\mathbf{m}_j)\right]^T \mathbf{C}_D^{-1} \left[\mathbf{d}_{obs} - \mathbf{g}(\mathbf{m}_j)\right].$$

(ii) When both the mean and the standard deviation of $\{S_d(\mathbf{m}_j)\}_{j=1}^{N_e}$ decrease, the value of $\lambda_\ell$ is reduced by a factor of 10 (i.e., $\lambda_{\ell+1} = \lambda_\ell/10$).

(iii) When only the mean of $\{S_d(\mathbf{m}_j)\}_{j=1}^{N_e}$ decreases, the value of $\lambda_\ell$ is unchanged.

(iv) When the mean of $\{S_d(\mathbf{m}_j)\}_{j=1}^{N_e}$ increases, the current model update is rejected and the value of $\lambda_\ell$ is enlarged by a factor of 10 (i.e., $\lambda_{\ell+1} = 10 \times \lambda_\ell$).

As to the stopping criteria, the iteration stops once the number of iterations exceeds a predefined maximum value of 15, or the reduction of the mean of $\{S_d(\mathbf{m}_j)\}_{j=1}^{N_e}$ between two successful adjacent iterations is less than 1%.

## Appendix B. Bootstrap sampling of Kalman gain

| **Algorithm** - Bootstrap sampling of Kalman gain |
| --- |
| 1. Set a random seed (for experimental repeatability) |
| 2. Start bootstrapping at the $\ell$th iteration of LM-EnRML: |
|     **for** $l = 1$ to $N_b$ **do** |
|         randomly resample $N_e$ ensemble members with replacement from $\mathbf{M}^\ell$ |
|         compute $\mathbf{K}^l$ according to Equation 7 or 11 using the resampled ensemble |
|     **end** |